Tenth International Conference on
Computational Fluid Dynamics (ICCFD10),
Barcelona, Spain, July 9–13, 2018

ICCFD10-2018-360

The second law of thermodynamics and the numerical simulation of transport phenomena with chemical reactions

Allen E. Ream, J. C. Slattery and P. G. A. Cizmas
Corresponding author: cizmas@tamu.edu

Texas A&M University, Department of Aerospace Engineering
College Station, TX 77843-3141, USA

Abstract: This paper explores the effect of the chemical kinetics and thermal diffusion models on the differential entropy inequality (DEI), the local form of the second law of thermodynamics. This analysis was done while simulating a laminar, premixed, simple jet methane-air flame, known as the Sandia flame A. By choosing a laminar flame, the modeling of turbulence and the inherent uncertainty associated with it were avoided. Five chemical kinetics mechanisms were considered; one detailed mechanism, the GRI 3.0 mechanism, and four reduced mechanism: Westbrook and Dryer, Jones Mech 2, and the optimized two- and three-step mechanisms. As expected, the detailed mechanism matched experimental data of the Sandia flame A quite well. The only exception was that the flame width was over-predicted by approximately 25%. This incorrect width could be due to the co-flow velocity used. The reduced mechanisms did a poor job of matching the experimental data due to excessively high upper flammability limits. Premature ignition was experienced which caused the inner surface of the flame to be artificially advanced towards the fuel tube. Once the initial oxygen supply was depleted, the reduced mechanism simulations exhibited similar responses to the GRI 3.0 mechanism since the flame is diffusion rate limited. Non-automatic satisfaction of the DEI was limited to only its chemical reaction term, as long as Fickian diffusion was used. Positive values for the species diffusion and heat transfer terms of the DEI were found when using Soret thermal diffusion coefficients. No violations of the DEI were found for the optimized two- and three-step mechanisms, just as they were designed to perform. The other two reduced mechanisms exhibited violations. Surprisingly, violations were found for the detailed GRI 3.0 mechanism. Potential sources could include an incomplete set of reactions, the inclusion of pressure-dependent elementary reactions, inaccurate rate parameters, or the numerical scheme used.

Keywords: Computational Fluid Dynamics, Combustion Modeling, Second Law of Thermodynamics, Reduced Kinetics Models, Thermal Diffusion.

1 Introduction

Computer hardware progress has led to the ability to solve complex transport phenomena using high fidelity numerical methods. In the case of reactive transport phenomena, the modeling of chemical reactions is of crucial importance for the accuracy of the results. The computational cost of modeling chemical reactions, however, is significant even for the simplest reactions. For example, modeling methane combustion requires 353 reactions with 53 species if the GRI 3.0 mechanism is being used. Adding 53 variables to the typical 7-component state variables, assuming compressible turbulent flow where two variables are used for turbulence modeling, dramatically increases the computational time. For this reason, it is common to use reduced kinetics models to lower the computational cost. There are issues, however, with using reduced kinetics models as they generate results that violate the second law of thermodynamics.

The current practice in the simulation of reactive transport phenomena is to formulate numerical methods that satisfy the mass, momentum and energy balance equations. The differential entropy inequality, the local form of the second law of thermodynamics, is always ignored in simulating chemically reacting flows. Ignoring the second law of thermodynamics for common types of material behavior, such as Newton's law of viscosity, Fourier's law, Fick's first law, is not an issue since they satisfy the differential entropy inequality automatically. Common empirical descriptions of chemical reactions, however, do not satisfy the differential entropy inequality automatically.

For the simulation of reacting fluid flows, it is necessary to incorporate a reaction mechanism that describes the incremental steps and associated rates leading from reactant species to products. To reduce the computational cost, reduced chemical kinetics mechanisms are used, which produce violations of the differential entropy inequality

$$-\mathrm{tr}\left[\left(\overline{\overline{\Pi}} + P\overline{\overline{I}}\right)\cdot\nabla\vec{v}\right] + c\hat{R}T\sum_{n=1}^{N_s}\vec{J}_{(n)}\cdot\frac{\vec{d}_{(n)}}{\rho_{(n)}} + \sum_{r=1}^{N_r}\sum_{n=1}^{N_s}\mu_{(n)}R_{(n)(r)} + \frac{1}{T}\vec{\epsilon}\cdot\nabla T \leq 0 \tag{1}$$

a local form of the second law of thermodynamics [1]. Here $\overline{\overline{\Pi}}$ is the stress tensor, P the thermodynamic pressure, $\overline{\overline{I}}$ the identity tensor, $\vec{v}$ the velocity vector, c the total molar density, $\hat{R}$ the gas law constant, T the temperature, N_s the number of species, $\vec{J}_{(n)}$ the mass flux of species n relative to $\vec{v}$, $\rho_{(n)}$ the mass density of species n, N_r the number of reactions, $\mu_{(n)}$ the chemical potential for species n on a molar basis, and $R_{(n)(r)}$ the rate of production of moles of species n per unit volume by homogeneous chemical reaction r. $\vec{\epsilon}$ is the energy flux corrected for the effects of mass transfer [2, p. 449]; $\vec{d}_{(n)}$ is the driving force for mass transfer corrected for temperature gradients and pressure gradients [2, p. 450].

Reduced chemical kinetics mechanisms are created to decrease the complexity and computational cost of a detailed mechanism. The simplifying assumptions used to create a reduced mechanism decreases the range of applicability of the resultant mechanism. For instance, the Westbrook and Dryer two-step mechanism was made to predict flame speed and flammability limits well, but has been shown to produce violations of the DEI. Using a theorem introduced in [1], reduced kinetics models were developed to eliminate or minimize the differential entropy inequality violations [3, 4].

In this paper, the results of simulating the Sandia flame A with five combustion mechanisms, including the detailed GRI 3.0 mechanism, are explored to compare the relative merits of each. The following section examines the numerical results generated using five different combustion mechanisms and compares them to experimental data. Violations of the DEI are discussed in section 5. The automatic satisfaction of each term of the DEI is investigated to discover the the root causes of DEI violations.

2 Physical Model

2.1 Governing Equations

The transport equations that govern the fluid flow are the mass, momentum, energy and species conservation equations. This section will briefly review these governing equations.

2.1.1 Mass Conservation

The conservation of mass equation, commonly referred to as the continuity equation, is given in its conservative form by

$$\frac{\partial\rho}{\partial t} + \nabla\cdot(\rho\vec{v}) = 0. \tag{2}$$

Here ρ is the fluid density and $\vec{v}$ is the velocity vector. This form of the equation assumes that the flow is unsteady and compressible.

2.1.2 Momentum Conservation

The momentum conservation equations, collectively referred to as the Navier-Stokes equations are:

$$\frac{\partial(\rho\vec{v})}{\partial t} + \nabla\cdot(\rho\vec{v}\vec{v}) = \nabla\cdot\overline{\overline{\Pi}} + \rho\vec{f}_b, \tag{3}$$

where $\overline{\overline{\Pi}}$ is the stress tensor, and $\vec{f}_b$ are the externally applied body forces. Body forces can be applied to individual species if desired by multiplying by the respective mass fraction and summing over all the species. The stress tensor includes contributions from both the thermodynamic pressure and viscous stresses

$$\overline{\overline{\Pi}} = \overline{\overline{\tau}} - P\overline{\overline{I}}, \tag{4}$$

where the viscous stress tensor is denoted as $\overline{\overline{\tau}}$, P is the thermodynamic pressure, and $\overline{\overline{I}}$ is the identity tensor. The viscous stress tensor is a symmetric tensor and is defined as

$$\overline{\overline{\tau}} = \mu \left(\nabla \vec{v} + \nabla \vec{v}^T \right) + \lambda \left(\nabla \cdot \vec{v} \right) \overline{\overline{I}}. \tag{5}$$

Here μ and λ are the dynamic and bulk viscosities respectively. Stokes' hypothesis is used to approximate the bulk viscosity as $\lambda = -\frac{2}{3}\mu$ [5, p. 67].

2.1.3 Energy Conservation

The energy equation, which can be written in many different forms depending on which parameters, is presented herein in the form used by FLUENT [6, pp. 133-4]. This form is preferred since FLUENT is the software package used for the simulations undertaken herein and because this form clearly shows the contributions from chemical reactions. The energy equation is given by

$$\frac{\partial (\rho e)}{\partial t} + \nabla \cdot \left(\vec{v} \left(\rho e + P \right) \right) = \nabla \cdot \left(k_{\text{eff}} \nabla T - \sum_{n=1}^{N_s} h_{(n)} \vec{J}_{(n)} + \left(\overline{\overline{\tau}}_{\text{eff}} \cdot \vec{v} \right) \right) + S_h, \tag{6}$$

where e is the the total mass specific energy, $h_{(n)}$ is the mass specific enthalpy of species n, k_{eff} is the effective thermal conductivity and $\overline{\overline{\tau}}_{\text{eff}}$ is the effective viscous stress tensor. $\vec{J}_{(n)}$ is the diffusive mass flux vector for species n and S_h is a source term given by [6, p. 136]

$$S_h = -\sum_{n=1}^{N_s} h^0_{f,(n)} R_{(n)},$$

where $h^0_{f,(n)}$ is the mole specific enthalpy of formation of species n and $R_{(n)}$ is the molar net rate of production of species n.

2.1.4 Species Conservation

For non-homogeneous and reacting flows, it is necessary to use the species conservation equations that model the motion of each constituent species

$$\frac{\partial \left(\rho Y_{(n)} \right)}{\partial t} + \nabla \cdot \left(\rho Y_{(n)} \vec{v} \right) = -\nabla \cdot \vec{J}_{(n)} + R_{(n)} M_{(n)}, \quad n = 1, \ldots, N_s - 1, \tag{7}$$

where $Y_{(n)}$ is the mass fraction of species n and $M_{(n)}$ is the molecular mass of species n. No new variables have been introduced in this equation, however a critical distinction must be noted. The density and velocity vector are both properties of the bulk flow while the mass fraction, diffusive mass flux vector, and net rate of production are all properties of individual species. This means that for each species to be included in the model an extra species equation needs to be included, up to a total of $N_s - 1$ species equations.

Since the system analyzed here had a nearly uniform pressure, the Dufour effect was neglected. We found no difference whether we included the Soret effect or not [4].

2.2 Chemistry Models

To simulate methane flame combustion, the detailed GRI 3.0 mechanism [7] and four reduced chemical kinetics models will be explored herein. The reduced chemical kinetics models are: (1) Westbrook and Dryer [8], Jones Mech 2 [3] and the optimized two- and three-step mechanisms [4]. The optimized two- and three-step mechanisms were obtained from the two-step Westbrook and Dryer mechanism [8] and the three-step Peters and Williams mechanism [9] using an optimization strategy to minimize the violations of the differential entropy inequality.

In a reactive system with N_s chemical species, any arbitrary reaction out of the N_r possibilities can be written as [10, p. 554-94].

$$\sum_{n=1}^{N_s} \nu'_{(n)(r)} \mathcal{M}_{(n)} \rightarrow \sum_{n=1}^{N_s} \nu''_{(n)(r)} \mathcal{M}_{(n)}, \quad r = 1, \ldots, N_r, \tag{8}$$

where $\mathcal{M}_{(n)}$ is the chemical symbol for species n and $\nu'_{(n)(r)}$ and $\nu''_{(n)(r)}$ are the stoichiometric coefficients for species n in reaction r as a reactant and a product, respectively. For this single reaction, it can be reasoned that the reaction rate is proportional to the rate of molecular collisions of reactant species and the energy of the collisions. The reaction rate equation which encompasses these ideas is given by the phenomenological law of mass action

$$\omega_{(r)} = k_{(r)} \prod_{n=1}^{N_s} c_{(n)}^{\nu'_{(n)(r)}}, \quad r = 1, \ldots, N_r. \tag{9}$$

Here $\omega_{(r)}$ is the volumetric molar progress of reaction r, $c_{(n)}$ is the molar concentration of species n, and $k_{(r)}$ is termed a reaction-rate constant. The progress of reaction r, only considering the forward reaction and allowing for non-stoichiometric concentration exponents, $q'_{(n)(r)}$, is given by

$$\omega_{(r)} = k_{(r)} \prod_{n=1}^{N_s} c_{(n)}^{q'_{(n)(r)}}, \quad r = 1, \ldots, N_r. \tag{10}$$

The molar rate of production of species n in reaction r, $R_{(n)(r)}$, is related to the progress of reaction through the stoichiometric coefficients from (8) through

$$R_{(n)(r)} = \left(\nu''_{(n)(r)} - \nu'_{(n)(r)}\right) \omega_{(r)}, \quad \begin{array}{c} n = 1, \ldots, N_s \\ r = 1, \ldots, N_r \end{array}. \tag{11}$$

The net molar production rate of species n, $R_{(n)}$, is found by summing the contributions from each reaction

$$R_{(n)} = \sum_{r=1}^{N_r} R_{(n)(r)} = \sum_{r=1}^{N_r} \left(\nu''_{(n)(r)} - \nu'_{(n)(r)}\right) \omega_{(r)}, \quad n = 1, \ldots, N_s. \tag{12}$$

To evaluate the progress of reaction, the reaction-rate constant $k_{(r)}$ is given by the empirical Arrhenius expression

$$k_{(r)} = A_{(r)} T^{\beta_{(r)}} \exp\left(\frac{-E_{a,(r)}}{\hat{R}T}\right), \quad r = 1, \ldots, N_r, \tag{13}$$

where $A_{(r)}$ is the Arrhenius pre-exponential constant, $\beta_{(r)}$ is the Arrhenius temperature exponent of reaction r, and $E_{a,(r)}$ is the activation energy of reaction r.

The Westbrook and Dryer mechanism is composed of two reactions with the second being reversible. It is beneficial to consider reversible reactions as two separate reactions so that the Arrhenius parameters for both the forward and reverse directions can be found independently. The resulting mechanism is shown in Table 1.

Table 1: Arrhenius Parameters of the Two-Step Westbrook and Dryer [8] Mechanism Split into All Forward Reactions.

Reaction	Equation	Arrhenius	Activation	Molar concentration exponent				
r		constant, $A_{(r)}$	energy, $E_{(r)}$	CH_4	O_2	CO	H_2O	CO_2
1	$CH_4 + 1.5O_2 \rightarrow CO + 2H_2O$	5.012×10^{11}	2.0×10^8	0.7	0.8			
2	$CO + 0.5O_2 \rightarrow CO_2$	2.239×10^{12}	1.7×10^8		0.25	1	0.5	
3	$CO_2 \rightarrow CO + 0.5O_2$	5×10^8	1.7×10^8					1

Units are cm, mol, cal, s, and K.

The Arrhenius parameters for the Jones Mech 2 and the optimized two-step and three-step mechanisms are shown in Tables 2-4.

Table 2: Arrhenius Parameters of Jones Mech 2 Mechanism [11, p. 103]

Reaction	Equation	A	β	E
1	$CH_4 + 1.5O_2 \rightarrow CO + 2H_2O$	1.5291×10^{13}	2.3077	6.0031×10^4
2_f	$CO + 0.5O_2 \rightarrow CO_2$	2.1685×10^8	−0.6022	-2.1560×10^1
2_b	$CO_2 \rightarrow CO + 0.5O_2$	1.4286×10^9	2.8571	1.7072×10^5

Units are cm, mol, cal, s, and K.

Table 3: Arrhenius Parameters of the Optimized Two-Step Mechanism [4].

Reaction	Equation	A	β	E
1	$CH_4 + 1.5O_2 \rightarrow CO + 2H_2O$	3.1623×10^{14}	0.8308	2.3855×10^4
2_f	$CO + 0.5O_2 \rightarrow CO_2$	4.2094×10^6	0.1251	7.3969×10^3
2_b	$CO_2 \rightarrow CO + 0.5O_2$	1.4286×10^9	0.2851	1.7072×10^5

Units are cm, mol, cal, s, and K.

Table 4: Arrhenius Parameters of the Optimized Three-Step Mechanism [4].

Reaction	Equation	A	β	E
1	$CH_4 + O_2 \rightarrow CO + H_2 + H_2O$	4.8801×10^{12}	0.4452	2.3849×10^4
2_f	$CO + H_2O \rightarrow CO_2 + H_2$	2.3037×10^{11}	−1.0206	2.3901×10^3
2_b	$CO_2 + H_2 \rightarrow CO + H_2O$	1.4286×10^{12}	0.2851	1.7072×10^5
3	$O_2 + 2H_2 \rightarrow 2H_2O$	1.0000×10^9	2.5903	1.1360×10^2

Units are cm, mol, cal, s, and K.

3 Numerical Model

The effect of the kinetics model on the differential entropy inequality was investigated using Fluent [12]. It was decided to use a commercial code as opposed to an in-house code such that other users can duplicate the results.

Sandia flame A, a laminar methane flame, was used in this investigation. By choosing a laminar flame, the modeling of turbulence and the inherent uncertainty associated with it were avoided.

3.1 Computational Domain

Flame A is a laminar, premixed, simple jet, methane-air flame used as a daily calibration target. In the Sandia flame A experiment a tube releases a premixed fuel mixture which stabilizes an attached flame at its exit. The flame can be considered attached when compared to a lifted flame. The tube is long enough to ensure that the velocity profile is fully developed at the exit plane. The fuel is premixed at an equivalence ratio considerably above the fuel's flammability limit. The fuel tube protrudes slightly from the end of a square wind tunnel which provides a low speed entraining flow of air referred to as the co-flow. The entire experiment is open to ambient conditions and the fuel and co-flow are at standard atmospheric temperature and pressure before combusting.

The setup is shown in Fig. 1. The entire setup was oriented vertically so that asymmetric effects on the flame due to gravity would be negligible. These experiments were open to ambient conditions so the flame can be considered isobaric. In the simulation, the square duct was approximated to be circular such that the model flame can be simplified to a two-dimensional problem [4].

3.2 Grid Generation

A hybrid, structured and unstructured grid was used to discretize the computational domain. A structured rectangular grid was used close to the center line to properly capture the boundary layers on the tube and wind tunnel walls. An unstructured grid was used in the free stream to decrease the number of cells where the resolution is less important. Four grids, with a number of cells ranging from 22,999 to 260,158, were generated to verify that the solution is grid independent. As illustrated in [13], a grid with 84,780 cells, shown in Fig. 2, was sufficient to yield a grid independent solution.

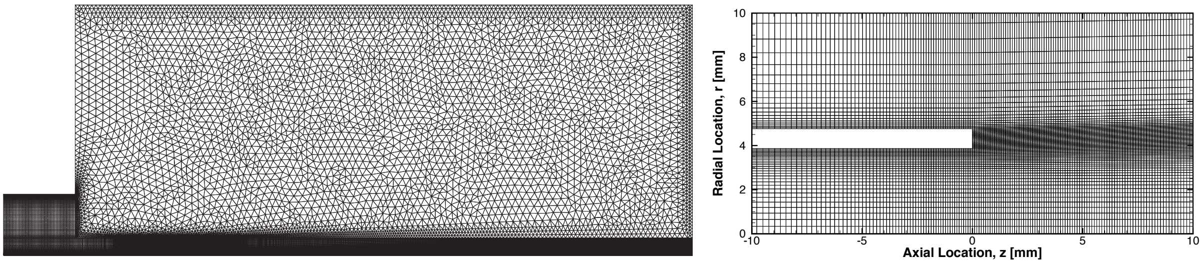

(a) (b)

Figure 2: Flame A mesh with 84,780 cells: (a) entire domain, (b) zoomed view at methane tube exit.

3.3 Boundary Conditions

Hard surfaces, such as the wind tunnel and the fuel inlet tube, were modeled as wall boundaries. All wall surfaces enforced no slip and no penetration of the flow adjacent to the wall. Thermally, the walls were modeled to allow no heat flux.

The inlet and outlet boundary conditions used in the simulation are given in Table 5.

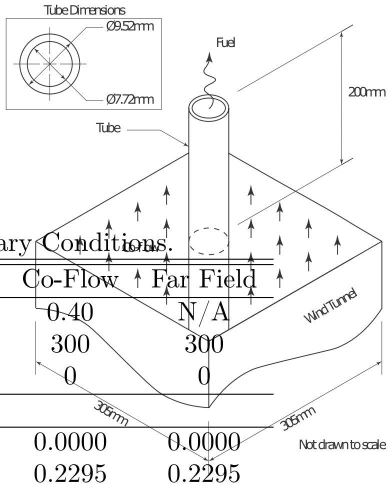

Figure 1: Isometric view of experimental setup for Sandia Flame A. All units are given in millimeters. Note that the drawing is not to scale.

Table 5: Inlet and Outlet Boundary Conditions.

Zone	Premixed Fuel	Co-Flow	Far Field
Velocity [m/s]	2.90	0.40	N/A
Temperature [K]	300	300	300
Gauge Pressure [Pa]	0	0	0
Species Mass Fractions			
CH_4	0.1528	0.0000	0.0000
O_2	0.1944	0.2295	0.2295
CO_2	0.0004	0.0005	0.0005
CO	0.0000	0.0000	0.0000
H_2O	0.0066	0.0078	0.0078
N_2	0.6458	0.7622	0.7622

4 Results

The Sandia flame A experiment was simulated using five different methane-air combustion mechanisms. These included the detailed GRI 3.0 mechanism, Westbrook and Dryer two-step mechanism, Jones Mech 2, and the optimized two- and three-step mechanisms. Before delving into violations of the DEI, it is useful to understand the structure of the resulting flames.

4.1 Temperature and Composition Contours

In all simulations of the Sandia flame A the temperature limiter was set to 2400 K, that is, well above the adiabatic flame temperature. This value was chosen to decrease in situ adaptive table (ISAT) [14] look-up time while not influencing the solution results. Therefore, the maximum temperature found in the results should be a numerical approximation of the adiabatic flame temperature.

Table 6 gives a comparison of the maximum temperature for each simulation along with predicted values for the adiabatic flame temperature and the calculated error. Since the adiabatic flame temperature is a function of the chemical species present, only mechanisms which include the same species can be directly compared. For all others, only a comparison of error is possible.

Table 6: Maximum Temperature of Various Mechanisms

Mechanism	Species Number	Adiabatic Flame Temp. [K]	Max Temp. [K]	Error [%]
GRI 3.0	53	2225.5	2268.0	+1.91
Westbrook & Dryer	6	2258.2	2305.4	+2.09
Jones Mech 2	6	2258.2	2229.2	-1.28
Optimized 2-step	6	2258.2	2311.2	+2.35
Optimized 3-step	7	2246.4	2261.0	+0.65

The maximum flame temperature error is less than 2.4% for each mechanism. For all mechanisms besides Jones Mech 2, the maximum temperature is higher than the predicted adiabatic flame temperature. Of all the six species models, Jones Mech 2 had the lowest error in temperature.

Figures 3 and 4 show contour plots of temperature and methane mass fraction respectively for each mechanism. A quick inspection shows that the basic structure of the flame for each mechanism is the same. Each flame contains a cool conic interior section of unburnt fuel, and a zone of maximum temperature which is approximately centered radially in the flame. Temperature gradients exist on the inside and outside surfaces of the flame and are where reactions are occurring most prominently.

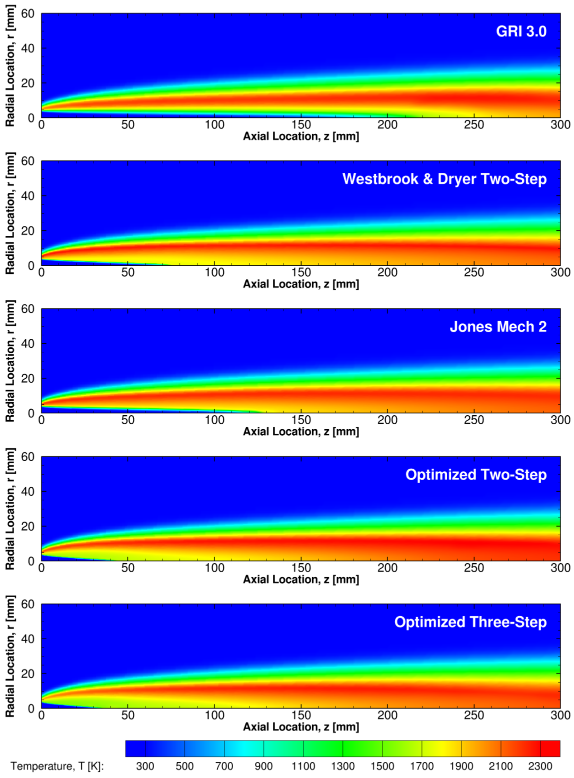

Figure 3: Temperature profiles of various mechanisms. From top to bottom: GRI 3.0 [15], Westbrook and Dryer two-step [8], Jones Mech 2 [11], optimized two-step, optimized three-step.

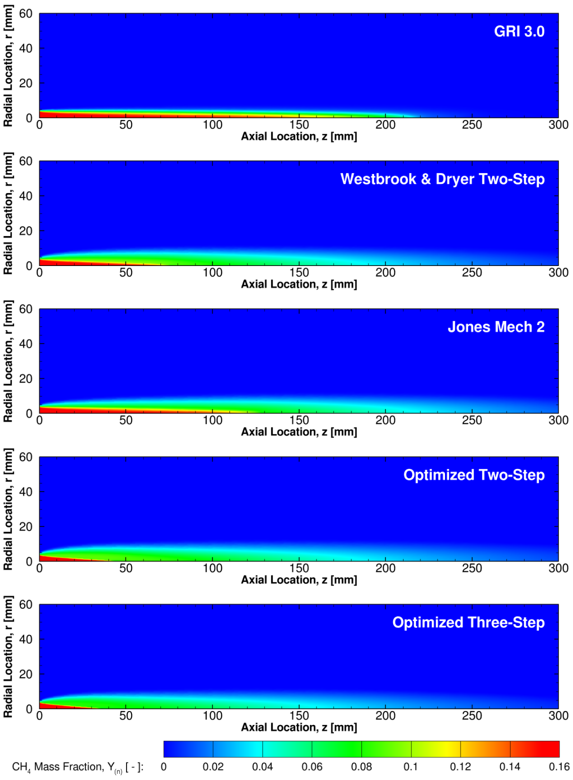

Figure 4: Methane (CH_4) mass fraction profiles of various mechanisms. From top to bottom: GRI 3.0 [15], Westbrook and Dryer two-step [8], Jones Mech 2 [11], optimized two-step, optimized three-step.

In both figures 3 and 4, it can be qualitatively seen that the cool interior section of the flame is a different length for each mechanism while the outer surfaces seem to occur in nearly the same location.

The experimental data were collected at 25, 50, and 100 mm downstream of the fuel tube exit. Clearly for some of the reduced mechanisms, the cool interior doesn't extend out 100 mm. Therefore, the largest differences in the solutions are expected to occur near the centerline of the flame, and indeed this is the case, as will be displayed in section 4.2.

An interesting phenomenon is found in the methane mass fraction profiles which may help explain the differences in structure of the flames. In Fig. 4 it can be seen that the unburnt fuel (shown in red on the contour plots) extends a variable distance into the flame. However, the distance at which the fuel is completely depleted is approximately 200 mm downstream and is nearly the same for each mechanism. The variable internal length is due to premature ignition of the premixed fuel and differences in reaction rates between the mechanisms. The nearly constant distance at which fuel depletion occurs is due to the oxygen diffusion rate being approximately constant between each simulation.

For all the reduced reactions the premixed oxygen is quickly depleted since the mixture is fuel rich and the single initiation reaction feeds directly on O_2. The rate of the initiation reaction determines the slope of the inner edge of the flame. The faster the reaction rate, the steeper the slope. Once the premixed oxygen is depleted, the overall reaction stagnates until enough oxygen can diffuse into the flame to react with the remaining fuel. Since the rate of oxygen diffusion is roughly the same for each simulation, the point at which the fuel runs out is nearly constant.

The length of the internal cool cone for the detailed GRI 3.0 mechanism is longer than for the reduced mechanisms since the initiation of the overall combustion is much more complex than for the reduced mechanisms. Unlike the reduced mechanisms which initiate with the reaction of CH_4 and O_2, the elementary initiation steps in the detailed mechanism require radical species to start the chain reaction. Since no radical species are present in the premixed fuel flow, the radical pool must first be established before the detailed mechanism can combust. Not until high enough oxygen concentrations diffuse into the flame can the radical pool grow to a sufficient size for the propagation and chain branching steps to drive the overall reaction to termination.

In previous studies the reduced mechanisms were made to behave more like the detailed mechanism by eliminating the oxidizer in the fuel flow [11, pp. 86-92]. In an attempt to get a three-step mechanism simulation to run properly, Jones experimented with removing the premixed oxygen from the fuel and replacing it with nitrogen. The resulting flame had an elongated interior cool section which better matched experimental data and more closely resembled the GRI 3.0 mechanism from Fig. 3. This result was due to the lack of oxidizers in the fuel stream to prematurely start the reactions. The reactions could only begin once enough oxygen had diffused into the flame. Since the diffusion rate was unaltered between these simulations, the resulting solutions appeared to match experimental data better. However, this was not due to mechanisms performance, but rather because the flame was diffusion limited and was being denied a premixed supply of oxygen.

4.2 Comparison to Experimental Data

Profiles of temperature and species mass fractions were taken for each of the five mechanisms at 25, 50, and 100 mm downstream of the fuel tube. These profiles were then plotted against the experimental Sandia flame A data shown in Figs. 5-7.

The GRI 3.0 mechanism, being the only detailed mechanism tested, was expected to match the experimental data the closest. This expectation was verified as shown in figures 5-7. Along the inner edge of the flame the GRI 3.0 mechanism matches the experimental data very well. This is particularly emphasized in Fig. 6 where the consumption of CH_4 is shown. At all three axial locations the curve for the GRI 3.0 mechanism falls almost directly on top of the experimental data. Very close agreement is found between the GRI 3.0 mechanism and the experimental data along the inner edge of the flame.

There is a wide variation in the structure of the inner edge of the flame predicted by the various reduced mechanisms. In the previous section it was theorized that this was due to a premature combustion of the premixed fuel. For the Sandia flame A experiment the equivalent ratio of the premixed fuel was 3.17, that is, the fuel mixture was chosen to be outside the flammability limits of the methane fuel. However, the flammability limits of the reduced mechanisms may not match the physical values. The optimized two- and three-step mechanisms, along with Jones Mech 2, were created to minimize the number of violations of the DEI seen in reduced mechanisms. Never in their creation were flammability limits considered [13]. Therefore, along the inner edge of the flame, premature combustion could be expected. Indeed, premature combustion is shown in the contours of each of the reduced mechanisms in figures 3 and 4 as a shortened interior cone of unburnt fuel compared to the GRI 3.0 mechanism.

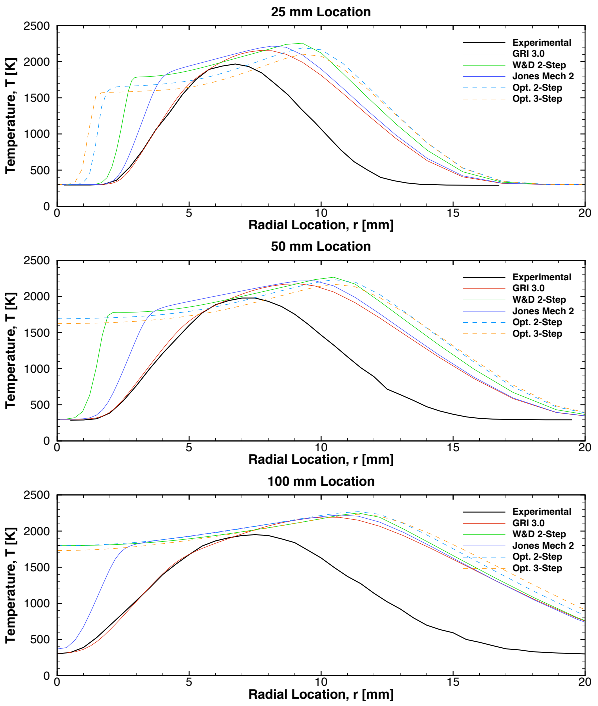

Figure 5: Comparison of temperature profiles to experimental data for all mechanisms. Profiles shown from top to bottom at: 25 mm, 50 mm, and 100 mm locations.

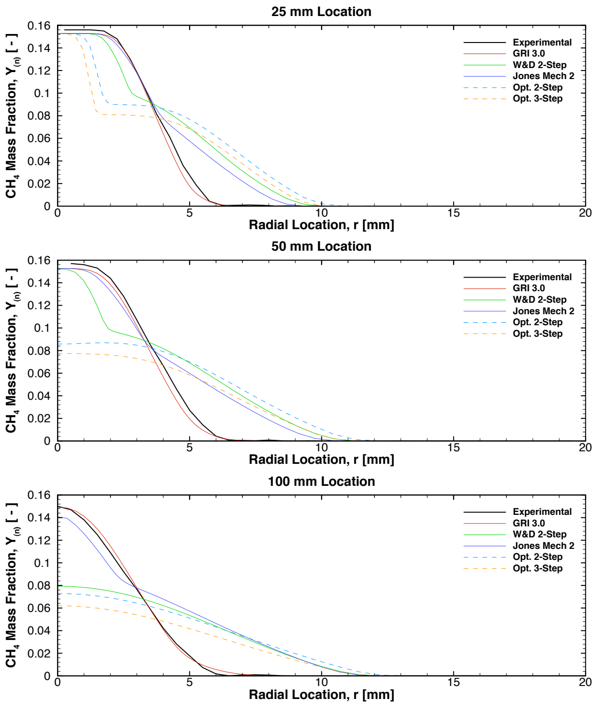

Figure 6: Comparison of CH_4 mass fraction profiles to experimental data for all mechanisms. Profiles shown from top to bottom at: 25 mm, 50 mm, and 100 mm locations.

The degree to which the interior cone of unburnt fuel was shortened for the reduced mechanisms was determined by the reaction rate of the fuel decomposition reaction. A faster reaction rate led to a shorter cone. It was predicted that the flame speed is proportional to the square root of the reaction rate [8]. Based on this relation, the optimized two- and three-step mechanisms were predicted to exhibit the shortest sections of unburnt fuel. Another way to view this is in the temperature profiles of Fig. 5. For the optimized two- and three-step mechanisms the temperature does not dip back to ambient at the center of the flame for the 50 mm and 100 mm sampling locations due to the shortened interior cone. Therefore, while the optimized two- and three-step mechanisms predict the flame speed most accurately, Jones Mech 2 appears to match the inner surface of the Sandia flame A more closely.

None of the five mechanisms tested show good agreement with the experimental data on the outside edge of the flame. For all mechanisms tested, the overall width of the flame was over-predicted by approximately 25%. While the detailed GRI 3.0 mechanism consistently showed the closest match to the experimental data on the outside edge of the flame, all of the reduced mechanisms also predicted very similar results to the detailed mechanism along the outer edge. This is best

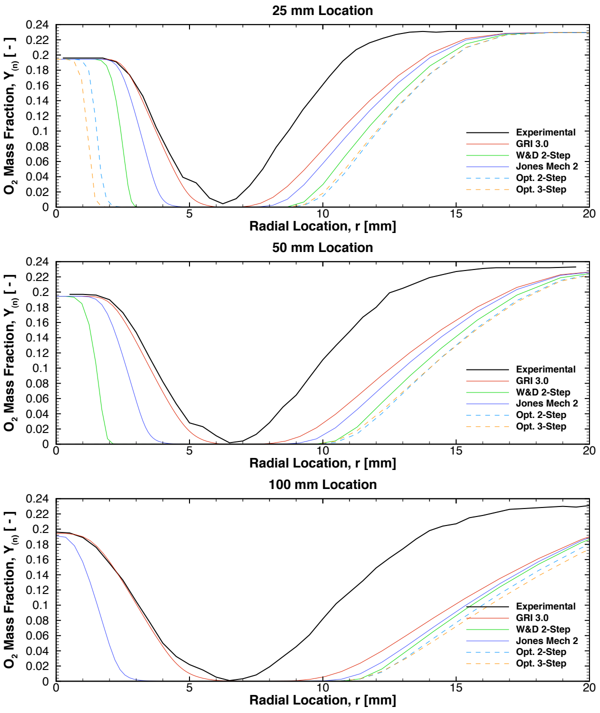

Figure 7: Comparison of O_2 mass fraction profiles to experimental data for all mechanisms. Profiles shown from top to bottom at: 25 mm, 50 mm, and 100 mm locations.

shown in the temperature profiles in Fig. 5 and the oxygen mass fraction profiles in Fig. 7. At the outside edge of the flame the profiles for all of the mechanisms seem to cluster together into one consistent curve which sits a considerable distance from the experimental data.

The similarities between all the solutions at the outside edge of the flame are due to the flame being diffusion rate limited. Since the fuel and oxygen supplies are on opposite sides of the flame, combustion can only occur when the fuel and oxygen have sufficiently diffused together. Diffusion occurs on a slower time scale than the reaction rates and the same diffusion model is used on all simulations. Therefore, the solutions at the outside edge of the flame should be very similar, regardless of reaction mechanism used.

The reason for the difference between the numerical simulations and the experimental data at the outer edge of the flame is most likely due to an error in the co-flow velocity. In all simulations the co-flow was taken to be 0.4 m/s. This value was first used by Chambers [16] and was established through an undocumented personal correspondence. However, documentation from Sandia [17] suggests that the actual co-flow velocity was 0.9 m/s. This is a substantial difference which could account for error between the numerical simulations and the experimental data. Further testing is required to determine if simulations with a co-flow of 0.9 m/s decreases the error at the outer edge of the flame.

4.3 Plateaued Structure of Reduced Mechanisms

In each of the plots in Fig. 5, there is a characteristic plateaued structure exhibited by each of the reduced mechanisms. Where the experimental data and the GRI 3.0 simulation have rounded temperature profiles, the reduced mechanisms are defined by nearly flat, slightly sloping temperature plateaus in the middle of the flame. This structure can be explained by the low number of species and lack of competing reactions in the reduced mechanism.

In a detailed mechanism, when the initiation reactions occur, the heat released goes into supplying the activation energy to fuel further reactions. Gradually, as the chain reactions progress, the overall temperature increases until a maximum is reached. For the reduced mechanisms, the heat released by the initiation reaction has no other reactions to supply so the temperature increases sharply. The temperature then remains relatively constant until the next reaction occurs. For many of the reduced mechanisms shown in Fig. 5 there are only two reactions so the temperature profiles are defined by two sharp gradients.

Figure 8 shows the reaction rates overlaid on the temperature profiles for the Westbrook and Dryer two-step mechanisms. It is clear from these plots that edges of the plateaued structure correspond with peaks in reaction rate. From the inside of the flame outward, the initial jump in temperature occurs where the first reaction spikes. At this location, the forward and reverse rates of the second reaction start to slowly increase until a peak in rates of production at the outer edge of the flame. The slight slope in the middle of the temperature profile is due to the heat release from the building forward and reverse rates of the second reaction.

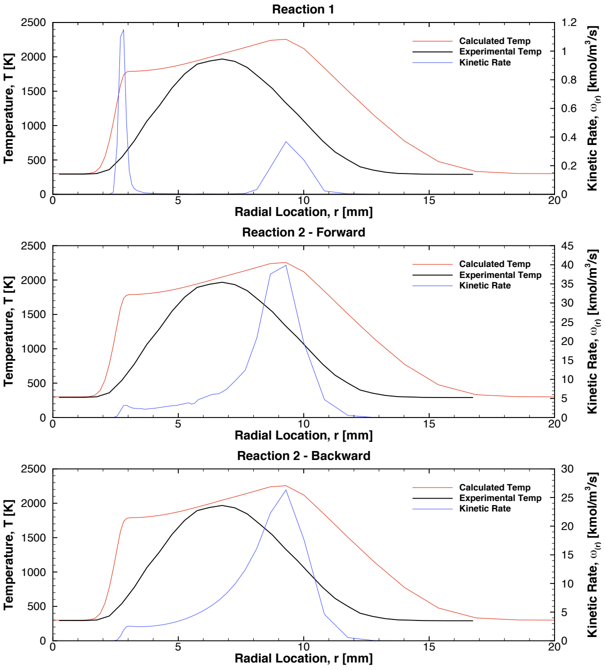

Figure 8: Plateaued temperature profile plotted next to kinetic rate for each reaction of Westbrook and Dryer two-step mechanism [8]. All data is captured at the 25 mm location.

5 DEI Violations

The DEI, (1), represents a local form of the second law of thermodynamics. For a CFD simulation of a reacting flow to be physically accurate it must satisfy the DEI at all points within the computational domain. However, as first noticed by Chambers [16, pp. 126-32], the DEI is violated at numerous locations for common reduced combustion mechanisms. No current CFD reacting flow solver implements the DEI as a solution limiter. Thus, combustion mechanisms should be used which automatically satisfy the DEI. The optimized two- and three-step mechanisms created in [4] were made in accordance with a theorem for automatic satisfaction given by Slattery et al. [1].

In the following sections, solutions of Sandia flame A calculated using various combustion mechanisms are analyzed for violations of the DEI. The mechanisms used are the optimized two- and three-step mechanisms [4], the Westbrook and Dryer two-step mechanism [18], Jones Mech 2 [3], and the detailed GRI 3.0 mechanism [7]. In the following sections, each term of the DEI is investigated separately to determine its contribution to the inequality (1).

5.1 First Term

The first term of the DEI, $-\mathrm{tr}\left[\left(\overline{\overline{\Pi}} + P\overline{\overline{I}}\right)\cdot\nabla\vec{v}\right]$, represents entropy generation due to viscous stresses. For the Sandia flame A, since the domain is of constant pressure, the largest viscous stresses are encountered along the solid wall surfaces of the fuel tube and wind tunnel. Since the velocity of the fuel is much greater than that of the co-flow, and since the diameter of the fuel tube is considerably smaller than that of the tunnel, the largest velocity gradients are expected to be within the fuel tube. Figure 9 shows a contour plot of the first term of the DEI inside the fuel tube calculated for the Westbrook and Dryer two-step mechanism [8]. The values of the first term are all negative.

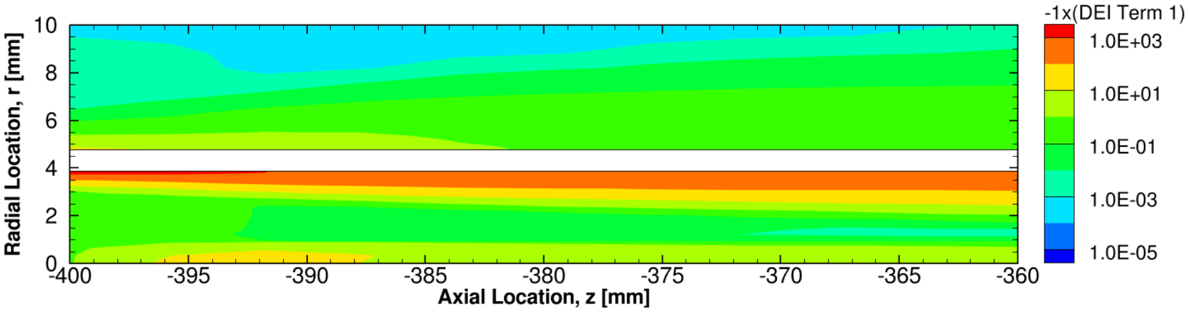

Figure 9: Contours plot of the first term of the DEI calculated for the Westbrook and Dryer two-step mechanism [8].

The condition for automatic satisfaction of the first term is that the fluid behaves as a compressible Newtonian fluid. No non-linear viscosity relationships were used in the numerical model so the first term was automatically satisfied in the solutions for each of the five mechanisms. It is interesting to note that the values of largest magnitude for the first term were found along the tube wall at the inlet boundary. This is due to the constant velocity profile that was used for this boundary condition. Boundary layers start to form along the inner wall of the tube which gives rise to large velocity gradients and viscous stresses at the velocity inlet. The large values of the first terms seen at this point are due to the boundary conditions.

5.2 Second Term

The second term of the DEI, $c\hat{R}T\sum_{n=1}^{N_s}\vec{J}_{(n)}\cdot\frac{\vec{d}_{(n)}}{\rho_{(n)}}$, represents the entropy generation due to species diffusion. The second term is primarily influenced by the temperature, gradients in composition, and the diffusion model used. The calculation of the diffusive mass flux vector, $\vec{J}_{(n)}$, is where the diffusion model makes an impact. For Fickian diffusion $\vec{J}_{(n)}$ is calculated using

$$\vec{J}_{(n)} = -\rho D_{(n),mix}\nabla Y_{(n)}, \quad n = 1,\ldots,N_s - 1 \tag{14}$$

where $D_{(n),mix}$ is the mass diffusion coefficient for species n into the mixture given by Wilke's formula [19]

$$D_{(n),mix} = \frac{1 - X_{(n)}}{\sum\limits_{\substack{m=1 \\ m\neq n}}^{N_s} \left(X_{(m)}/\mathcal{D}_{(n)(m)}\right)}, \tag{15}$$

where $X_{(n)}$ is the mole fraction of species n. $D_{(n)(m)}$, the binary diffusion coefficients of species n into species m, are calculated using a modification of the Chapman-Enskog formula [20, p. 511]

$$\mathcal{D}_{(n)(m)} = 0.0018583 \frac{\left[T^3\left(\frac{1}{M_{(n)}} + \frac{1}{M_{(m)}}\right)\right]^{1/2}}{P\sigma^2_{(n)(m)}\Omega_{D,(n)(m)}}, \qquad \begin{array}{c} n = 1,\ldots,N_s \\ m = 1,\ldots,N_s \end{array} . \tag{16}$$

P is the pressure, $\sigma_{(n)(m)}$ is the Lennard-Jones parameter and $\Omega_{\mathcal{D},(n)(m)}$ is the diffusion collision integral.

For solutions that cannot be assumed to be dilute, a multicomponent and thermal diffusion model must be used. The calculation of the diffusive mass flux vector for species n then becomes [21, p. 458]

$$\vec{J}_{(n)} = -\sum_{m=1}^{N_s-1} \rho D_{(n)(m)} \nabla Y_{(m)} - D_{T,(n)}\frac{\nabla T}{T}, \quad n = 1,\ldots,N_s - 1 \tag{17}$$

where $D_{T,(n)}$ is the Soret thermal diffusion coefficient of species n [21, p. 456]

$$D_{T,(n)} = -2.59\times10^{-7} T^{0.659} \left(\frac{M_{(n)}^{0.511} X_{(n)}}{\sum\limits_{m=1}^{N_s} M_{(m)}^{0.511} X_{(m)}} - Y_{(n)} \right) \cdot \left(\frac{\sum\limits_{m=1}^{N_s} M_{(m)}^{0.511} X_{(m)}}{\sum\limits_{m=1}^{N_s} M_{(m)}^{0.489} X_{(m)}} \right), \quad n = 1,\ldots,N_s. \tag{18}$$

Entropy production from the second term is expected to occur all throughout the flame where the temperature is elevated and composition gradients are large due to chemical reactions. Figure 10 shows the contour plots of the second term of the DEI calculated for the Westbrook and Dryer two-step mechanism. The largest rate entropy generation from species diffusion is found along the edges of the flame where reactions are occurring most rapidly. This is due to the large heat release and change in chemical composition at these locations.

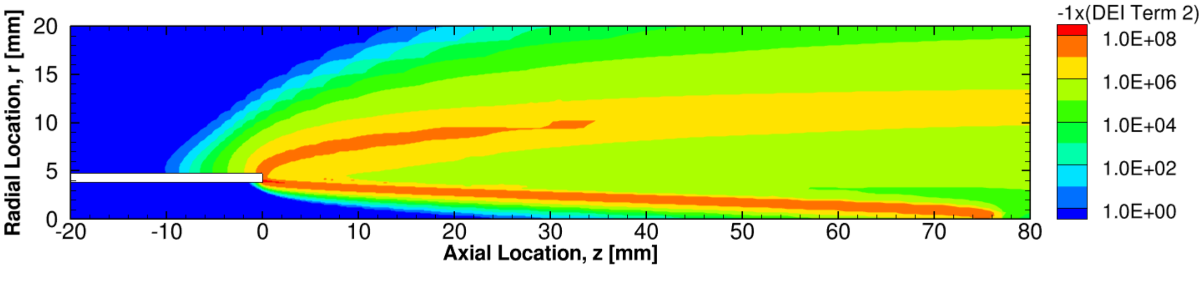

Figure 10: Contours plot of the second term of the DEI calculated for the Westbrook and Dryer two-step mechanism using diffusion given by (14).

The necessary conditions for automatic satisfaction of the second term are for the fluid to be a mixture of dilute gases which obey Fick's Law. Using Fickian diffusion coefficients and calculating $\vec{J}_{(n)}$ with (14) resulted in negative values in all cells of the computation domain. Since all necessary conditions for automatic satisfaction were met by the model used, no positive cells should have been encountered. This result was a good verification that the diffusion coefficients were being calculated correctly.

A separate set of simulations were run using multicomponent and thermal diffusion. Multicomponent and thermal diffusion coefficients are a higher-order model of diffusion which should yield improved results. These models, however, do not meet the necessary conditions for automatic satisfaction of the DEI. Table 7 gives the number of cells with positive second terms. Figure 11 shows the location and magnitude of the cells with positive second terms.

Table 7: Positive Second Terms Generated with Soret Diffusion Coefficients.

Mechanism	Number of Cells	Maximum Value [W/m^3]
GRI 3.0	6712	1.38×10^{-5}
Westbrook & Dryer	9792	1.36×10^{-5}
Jones Mech 2	9969	1.36×10^{-5}
Optimized 2-step	6880	1.36×10^{-5}
Optimized 3-step	4100	1.36×10^{-5}

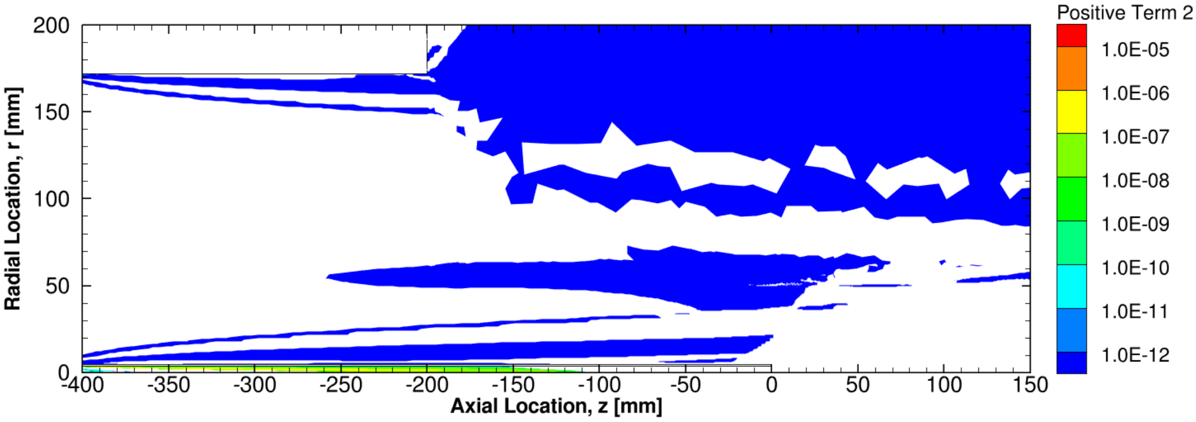

Figure 11: Contours plot of the cells with positive second term of the DEI, calculated for the Westbrook and Dryer two-step mechanism using diffusion given by (17).

Figure 11 shows that all positive cells were found well away from the reaction zone. In these areas the gradients in temperature and concentration were very small and entropy generation was negligible. Therefore, the small influence of the thermal diffusion coefficients allowed the second term to become slightly positive in these low gradient areas. The presence of positive values in the second term was due to the inclusion of the multicomponent and thermal diffusion coefficients. However, the magnitude of the positive values was influenced by two additional sources.

First, since this was a numerical simulation, there were bound to be minor inaccuracies in the results. In areas where the gradients were small the error in the calculated gradients could be of the same order of magnitude as the gradients themselves leading to inaccuracies in the second term calculation. The bulk of the positive cells were found downstream of the wind tunnel edge. At that location, the mesh transitions from structured to unstructured and the aspect ratios of the cells experience a sharp transition. Numerically this was not ideal and errors could manifest in the solution. In Table 7 the number of cells and maximum value were approximately equal for all simulations. The reason was because the second term is related to species diffusion and not chemical reactions. Since the same diffusion model was used for each simulation, the results should have been the same. The differences in number of positive cells was also due to the slight numerical errors in the low gradient areas of the grid.

Second, the largest magnitude positive values found when using multicomponent and thermal diffusion coefficients were located in the fuel tube. In the tube there was a slight pressure gradient due to the viscosity of the fuel flow. The calculation of the driving force for mass transfer vector, $\vec{d}$, assumed the flow to be isobaric. The small pressure gradient in the tube could have caused the calculated values to be slightly incorrect.

5.3 Third Term

The third term of the DEI, $\sum_{r=1}^{N_r} \sum_{n=1}^{N_s} \mu_{(n)} R_{(n)(r)}$, represents the entropy generation due to chemical reactions. The requirements for automatic satisfaction are that the fluid is a mixture of dilute gases and that all reactions in the mechanism are reversible and conform to the law of mass action. For reduced mechanisms, this is generally not the case, so it is expected that the third term could have positive values. Table 8 summarizes the values of the third term for each mechanism and Fig. 12 shows contour plots of the positive cells for each of the mechanisms.

Table 8: Positive Third Term Values.

Mechanism	Number of Cells	Maximum Value [W/m^3]
GRI 3.0	6713	5.81×10^7
Westbrook & Dryer	23887	1.40×10^9
Jones Mech 2	12679	1.86×10^6
Optimized 2-step	3479	1.42×10^1
Optimized 3-step	0	-

The profiles of positive values for each of the mechanisms shown in Fig. 12 all share a similar structure. Positive values are found all throughout the center of the flame with sharp boundaries at the inside and outside edges. Positive values only occur where reactions are taking place and appear to be of largest magnitude near the central axis of the flame. The profile for the optimized two-step mechanism is noticeably more sparse than the other mechanisms. This is also reflected in the values from Table 8.

The Westbrook and Dryer two-step mechanism had the largest number of positive cells and the largest positive values. This was expected since the Westbrook and Dryer mechanism has only two reactions and the concentration exponents are not the stoichiometric coefficients. The optimized two- and three-step mechanisms had the least number of positive cells with the three-step mechanism having none at all. While the optimized two-step mechanism had some positive cells, the maximum value seen was five orders of magnitude smaller than any of the other mechanisms. This was an encouraging result since the optimized two- and three-step mechanisms were specifically created to minimize this value.

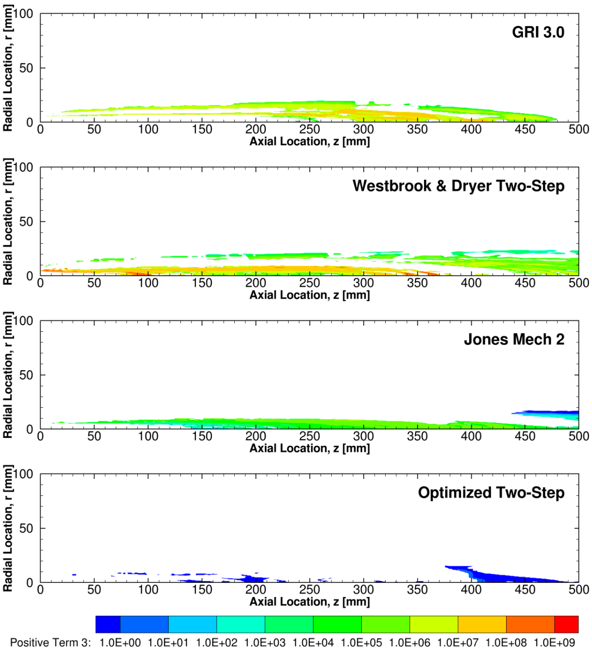

Figure 12: Contours plot of cells with positive third term. From top to bottom: GRI 3.0, Westbrook and Dryer two-step, Jones Mech 2, optimized two-step. The optimized three-step mechanism had no cells with positive third terms.

Unexpectedly, the detailed GRI 3.0 mechanism had a considerable number of positive third term cells. While positive values of the individual terms are allowed, as long as the sum total is negative, such large values for a single term are an indication that DEI violations may occur. One possible explanation for the positive cells is that the GRI 3.0 mechanism is not truly a complete mechanism. For the case tested here this is actually quite possible. FLUENT has an upper bound of 50 chemical species and the GRI 3.0 mechanism contains 53. Therefore, the minor species Ar, C_3H_7, and C_3H_8 were removed. These were chosen because they are either inert or related to propane combustion which was not found in Sandia flame A.

An incomplete mechanism could potentially cause the positive values seen, however, the magnitudes of the positive values for the optimized two- and three-step mechanisms, as well as Jones Mech 2, were considerably lower. All three of these reduced mechanisms were clearly incomplete and had at least one non-reversible reaction. Therefore, another likely reason would be that the GRI 3.0 mechanism contains a few pressure-dependent reactions which do not meet the necessary conditions for automatic satisfaction of the third term. While only a small number of elementary reactions are pressure-dependent, those that are directly deal with the decomposition of the methane fuel and play a large role in the overall reaction.

Another cause of the positive third term values for the GRI 3.0 mechanism is that the rate parameters are only order-of-magnitude estimates for many of the elementary reactions which deal with minor species. The error in the rates which control the minor species, while individually small, could accumulate to a sizable value when all the reactions are considered.

5.4 Fourth Term

The fourth term of the DEI, $\vec{\epsilon}\cdot\nabla T/T$, represents the entropy generation due to heat transfer. Since temperature gradients drive heat transfer, the largest magnitude of entropy generation is anticipated to be found where the temperature gradients are the steepest. Figure 13 shows the contours plot of the fourth term calculated using the Westbrook and Dryer two-step mechanism. The largest entropy generation is encountered along the inner surface of the flame. From Fig. 8 it is shown that, for this mechanism, the steepest temperature gradient is found in the same area, confirming the prediction. Along the outside edge of the flame the gradient is not as steep so the entropy generation is lessened.

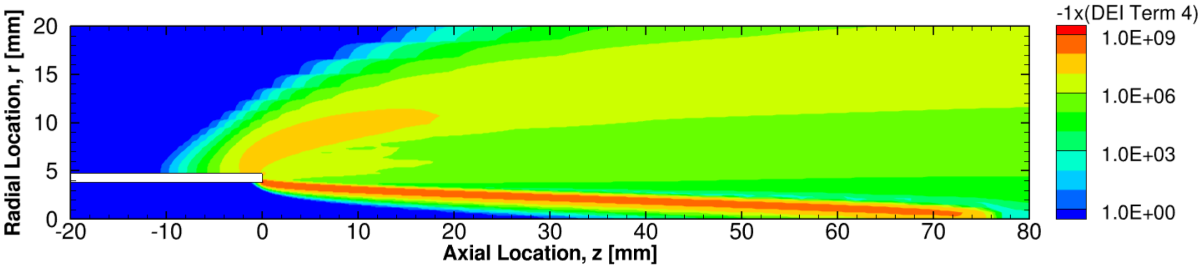

Figure 13: Contours plot of the fourth term of the DEI calculated for the Westbrook and Dryer two-step mechanism.

The conditions for automatic satisfaction of the fourth term are for the fluid to obey Fourier's Law of heat conduction. The numerical model assumed this behavior for all species so no positive values were predicted. However, the thermal diffusion coefficients that caused the positive second term values are also used in the calculate of the energy flux vector, $\vec{\epsilon}$

$$\vec{\epsilon} = -k\nabla T - c\hat{R}T\sum_{n=1}^{N_s} D_{T,(n)}\frac{\vec{d}_{(n)}}{\rho_{(n)}}. \tag{19}$$

where k is the thermal conductivity, which for an ideal gas mixture is calculated as a combination of kinetic theory and ideal-gas mixing law using Wassiljewa's equation

$$k = \sum_{n=1}^{N_s}\frac{X_{(n)}k_{(n)}}{\sum_{m=1}^{N_s} X_{(m)}\phi_{(n)(m)}}$$

with the Mason and Saxena function $\phi_{(n)(m)}$ [22, p. 10.31]. The individual species thermal conductivities, $k_{(n)}$, are calculated from kinetic theory by the equation [23, p. 534]

$$k_{(n)} = \frac{15}{4}\frac{\hat{R}}{M_{(n)}}\mu_{(n)}\left[\frac{4}{15}\frac{c_{p,(n)}M_{(n)}}{\hat{R}} + \frac{1}{3}\right], \quad n = 1,\ldots,N_s$$

where $\mu_{(n)}$ is the dynamic viscosity of species n calculated from kinetic theory, and $c_{p,(n)}$ is the specific heat of species n calculated from a polynomial curve fit.

In all simulations with the thermal diffusion coefficients turned off, each cell resulted in a negative value for the fourth term; all in accordance with the terms for automatic satisfaction. When the thermal diffusion coefficients were turned on, a few non-satisfying cells were found for each mechanism. A comparison of the number of non-satisfying cells, and magnitudes of the positive values, is shown in Table 9 for simulations using the thermal diffusion coefficients.

In each simulation using the thermal diffusion coefficients, the positive values for the fourth term are found along the inner edge of the flame as shown in Fig. 14. While some of the simulations only have one or two positive cells, they are always found at the forefront of the inner edge of the flame. Much like the second term, the positive values for the fourth term are all found in areas of low gradients where the slight effect of the thermal diffusion coefficients are most noticeable. The fourth term has an additional sensitivity to low temperatures due to the leading $1/T$ dependence which enhances the magnitude of the positive values of the fourth term.

Table 9: Positive Fourth Term Values for the Cases that Included Thermal (Soret) Diffusion Coefficients.

Mechanism	Number of Cells	Maximum Value
GRI 3.0	830	1.26×10^{3}
Westbrook & Dryer	2	1.67×10^{1}
Jones Mech 2	13	3.29×10^{1}
Optimized 2-step	1	8.43×10^{-1}
Optimized 3-step	377	6.88×10^{1}

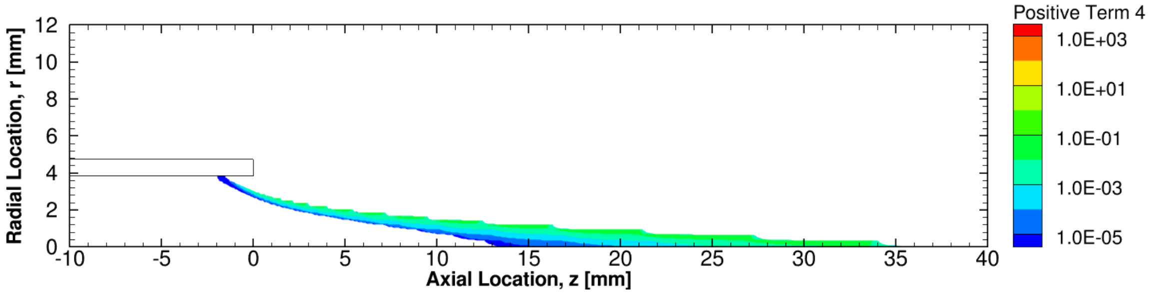

Figure 14: Contours plot of the cells with positive fourth term calculated for the GRI 3.0 mechanism and including thermal diffusion coefficients.

5.5 Entropy Violations

To verify whether the DEI is verified, the four terms of (1) are summed at every grid point. Positive values of any term individually were acceptable as long as the sum total was negative. However, for three of the five mechanisms investigated, the non-satisfying values of the third term were too large to be balanced by the other terms and violations of the DEI were found. Table 10 outlines the violations of the DEI found for each chemical mechanism.

Table 10: Violations of the DEI for Various Mechanisms.

Mechanism	Without thermal diffusion			With thermal diffusion	
	Number of Cells	Volume Fraction [%]	Maximum Positive Value	Number of Cells	Maximum Positive Value
GRI 3.0	3513	3.98×10^{-3}	5.72×10^{7}	4697	8.07×10^{7}
Westbrook & Dryer	20653	3.62×10^{-2}	1.40×10^{9}	23506	1.56×10^{9}
Jones Mech 2	2075	1.15×10^{-3}	1.71×10^{6}	2474	1.23×10^{6}
Optimized 2-step	0	0	-	0	-
Optimized 3-step	0	0	-	0	-

The optimized two- and three-step mechanisms performed exactly as they were intended, producing no violations of the DEI. Jones Mech 2 and the detailed GRI 3.0 mechanism both contained a small number of violating cells while, the Westbrook and Dryer two-step mechanism contained the most, and largest magnitude, violating cells. The Westbrook and Dryer mechanism was expected to produce the largest number of violations since it met none of the criteria for automatic satisfaction of the third term given in [1].

Figure 15 shows contours of violations of the DEI for the three violating mechanisms. Since only the third term had non-automatically satisfying cells, the plots in Fig. 15 look remarkable similarity to those in Fig. 12, where the non-satisfaction of the third term is shown. Comparing the number of DEI violations in Table 10 to the number of positive third term cells in Table 8, it is seen that the number of DEI violations was less than the number of positive third term cells. This indication that some of the non-satisfying cells for the third term were balanced by the negative values of the other terms. However, the magnitude of the third term positive values were simply too great to be balanced in all cells.

For each of the mechanisms there is a channel, centrally located in the flame, where violations do not occur. The top pane of Fig. 16 shows the DEI violations for the Westbrook and Dryer mechanism where

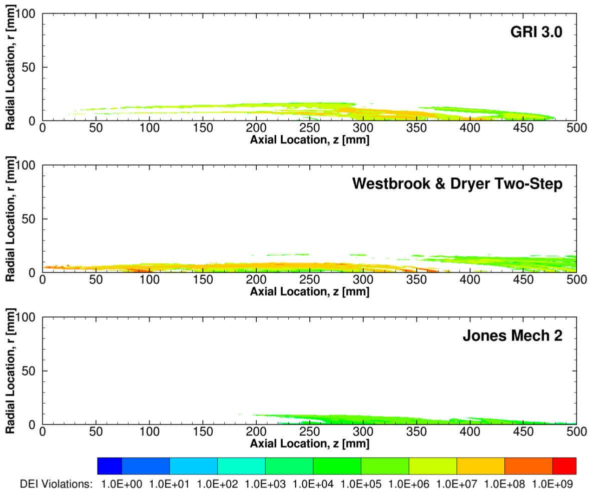

Figure 15: Profiles of entropy violations for various mechanisms. From top to bottom: GRI 3.0 [15], Westbrook and Dryer two-step [8], Jones Mech 2 [11]. The optimized two- and three-step mechanisms had no violating cells.

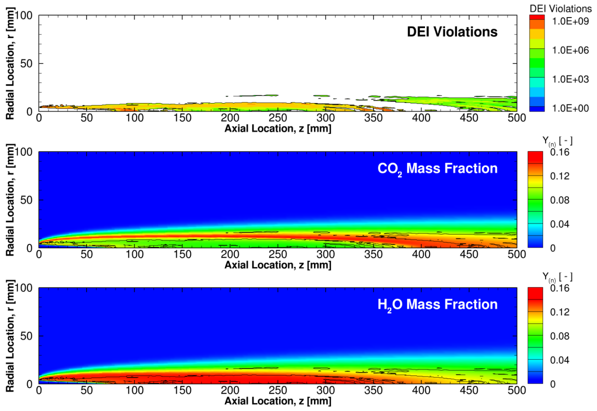

Figure 16: Outline of the entropy violations superimposed over contour plots of the major species product species CO_2 and H_2O for the Westbrook and Dryer two-step mechanism [8].

this channel is most prominently displayed. A bounding line has been drawn around the contours to show where the values transition from negative to positive. In the second and third panels this bounding line has been superimposed over mass fraction contours for CO_2 and H_2O. The gap in the DEI violations lines up exceedingly well with the areas where these product species are at their highest concentrations. Violations occur much more prevalently where reactions are occurring, or in other words, where the global reaction has not moved completely to product species. This could also support the theory that violations of the GRI 3.0 mechanism are due to the inaccurate rate parameters for the minor species reactions.

The most surprising result from this study was that the detailed GRI 3.0 mechanism still produced violations of the DEI. Equally intriguing was that the GRI 3.0 mechanism was used as the optimization target for creating the optimized two- and three-step mechanisms; both of which produced no violations. Previously discussed were the possibilities that the violations from the GRI 3.0 mechanism could be due to an incomplete combustion mechanism, pressure-dependent elementary reaction rates, or inaccurate rate parameters. Another possible cause could be that the numerical solution scheme imparted these violations. In previous studies where the Stiff Chemistry Solver was not used, Jones Mech 2 produced no violations of the DEI [11, p. 113]. In the current study, using the Stiff Chemistry Solver, Jones Mech 2 was found to produce 2075 violating cells. While this was still a very low number of violations, it was on par with the 3513 violations of the GRI 3.0 mechanism. Unfortunately, it was impossible to produce a converged solution of the GRI 3.0 mechanism without using the Stiff Chemistry Solver.

6 Summary

The structure of the Sandia flame A predicted by the detailed GRI 3.0 mechanism was found to match the experimental results quite well. The only exception was that the flame width was over-predicted by approximately 25%. This incorrect width could be due to the co-flow velocity used. The reduced mechanisms did a poor job of matching the experimental data due to excessively high upper flammability limits. The premixed fuel supply, while outside the flammability limits of actual methane fuel, was well within the acceptable range of the reduced mechanisms. Therefore, premature ignition was experienced which caused the inner surface of the flame to be artificially advanced towards the fuel tube. Once the initial oxygen supply was depleted, the reduced mechanism simulations exhibited similar responses to the GRI 3.0 mechanism since the flame is diffusion rate limited. The plateaued temperature profile of the reduced mechanisms was shown to be due to a lack of competing chemical reactions.

Non-automatic satisfaction of the DEI was limited to only the third term, as long as Fickian diffusion was used. Positive values for the second and fourth terms of the DEI were found when using Soret thermal diffusion coefficients. Soret diffusion accounts for counter gradient effects and does not meet the conditions for automatic satisfaction of the second and fourth terms. No violations of the DEI were found for the optimized two- and three-step mechanisms, just as they were designed to perform. Surprisingly, violations were found for the detailed GRI 3.0 mechanism. Potential sources could include an incomplete set of reactions, the inclusion of pressure-dependent elementary reactions, inaccurate rate parameters, or even the numerical scheme used.

Acknowledgments

The authors gratefully acknowledge the computational resources provided by the Texas A&M Supercomputing Facility.

References

[1] John C. Slattery, Paul G. A. Cizmas, Adonios N. Karpetis, and Steven B. Chambers. Role of differential entropy inequality in chemically reacting flows. *Chemical Engineering Science*, 66(21):5236–5243, 2011.

[2] J. C. Slattery. *Advanced Transport Phenomena.* Cambridge University Press, 1999.

[3] N. H. Jones, P. G. A. Cizmas, and J. C. Slattery. Creating reduced kinetics models that satisfy the entropy inequality. *Journal of Engineering for Gas Turbines and Power*, 137(7):071504–1–071504–9, July 2015.

[4] A. E. Ream, J. C. Slattery, and P. G. A. Cizmas. A method for generating reduced-order combustion mechanisms that satisfy the differential entropy inequality. *Physics of Fluids*, 30(4), 2018.

[5] Frank M. White and Isla Corfield. *Viscous Fluid Flow.* McGraw-Hill New York, 3rd edition, 2006.

[6] ANSYS Inc. *ANSYS Fluent Theory Guide*, 15.0 edition, 2013.

[7] Gregory P. Smith, David M. Golden, Michael Frenklach, Nigel W. Moriarty, Boris Eiteneer, C. Thomas Bowman Mikhail Goldenberg, Ronald K. Hanson, Soonho Song, Jr. William C. Gardiner, Vitali V. Lissianski, and Zhiwei Qin. GRI-Mech 3.0. http://www.me.berkeley.edu/gri_mech, 2012. accessed July 24, 2012.

[8] Charles K. Westbrook and Frederick L. Dryer. Simplified Reaction Mechanisms for the Oxidation of Hydrocarbon Fuels in Flames. *Combustion Science and Technology*, 27:31–43, 1981.

[9] N. Peters and F. A. Williams. The asymptotic structure of stoichiometric methane-air flames. *Combustion and Flame*, 68:185–207, 1987.

[10] Forman A. Williams. *Combustion Theory.* The Benjamin/Cummings Publishing Company, Inc., 2nd edition, 1985.

[11] N. H. Jones. The Importance of the Entropy Inequality on Numerical Simulations Using Reduced Methane-Air Reaction Mechanisms. Master's thesis, Texas A&M University, August 2012.

[12] ANSYS Inc. *ANSYS Fluent*, 15.0 edition, 2013.

[13] Allen E. Ream. Creating reduced order methane-air combustion mechanisms that satisfy the differential entropy inequality. Master's thesis, Texas A&M, College Station, Texas, December 2015.

[14] S. B. Pope. Computationally efficient implementation of combustion chemistry using in situ adaptive tabulation. *Combustion Theory and Modeling*, 1:41–63, 1997.

[15] G. P. Smith, D. M. Golden, M. Frenklach, B. Eiteener, M. Goldenberg, C. T. Bowman, R. K. Hanson, W. C. Gardiner, V. V. Lissianski, and Z. W. Qin. GRI-Mech 3.0, 2000. http://combustion.berkeley.edu/gri-mech/.

[16] S. B. Chambers. Investigation of Combustive Flows and Dynamic Meshing in Computational Fluid Dynamics. Master's thesis, Texas A&M University, December 2004.

[17] Sandia National Laboratories, "International Workshop on Measurement and Computation of Turbulent and Nonpremixed Flames," 2014, http://www.sandia.gov/TNF/abstract.

[18] C. K. Westbrook and F. L. Dryer. Simplified reaction mechanisms for the oxidation of hydrocarbon fuels in flames. *Combustion Science and Technology*, 27:31–43, 1981.

[19] C. R. Wilke. Diffusional properties of multicomponent gases. *Chemical Engineering Progress*, 46(2):95–104, 1950.

[20] R. B. Bird, W. E. Steward, and E. N. Lightfoot. *Transport Phenomena.* John Wiley & Sons Inc., New York, 1960. Second printing, 1962, with corrections.

[21] ANSYS Inc. *ANSYS Fluent User's Guide*, 15.0 edition, 2013.

[22] B. E. Poling, J. M. Prausnitz, and J. P. O'Connell. *The Properties of Gases and Liquids.* McGraw-Hill, fifth edition, 2001.

[23] J. O. Hirschfelder, C. F. Curtiss, and R. B. Bird. *Molecular Theory of Gases and Liquids.* Wiley, 1954. Second printing.